Inorganic Chemistry

Article

pubs.acs.org/IC

Electrochemical, Spectroscopic, and Density Functional Theory Characterization of Redox Activity in Nickel-Substituted Azurin: A Model for Acetyl-CoA Synthase

Anastasia C. Manesis and Hannah S. Shafaat*

Newman & Wolfrom Laboratory of Chemistry, The Ohio State University, 100 West 18th Avenue, Columbus, Ohio 43210, United States

Supporting Information

ABSTRACT: Nickel-containing enzymes are key players in global hydrogen, carbon dioxide, and methane cycles. Many of these enzymes rely on Ni^{I} oxidation states in critical catalytic intermediates. However, due to the highly reactive nature of these species, their isolation within metalloenzymes has often proved elusive. In this report, we describe and characterize a model biological Ni^{I} species that has been generated within the electron transfer protein, azurin. Replacement of the native copper cofactor with nickel is shown to preserve the redox activity of the protein. The $Ni^{II/I}$ couple is observed at −590 mV versus NHE, with an interfacial electron transfer rate of 70 s^{-1}. Chemical reduction of Ni^{II}Az generates a stable species with strong absorption features at 350 nm and a highly anisotropic, axial EPR signal with principal *g*-values of 2.56 and 2.10. Density functional theory calculations provide insight into the electronic and geometric structure of the Ni^{I} species, suggesting a trigonal planar coordination environment. The predicted spectroscopic features of this low-coordinate nickel site are in good agreement with the experimental data. Molecular orbital analysis suggests potential for both metal-centered and ligand-centered reactivity, highlighting the covalency of the metal−thiolate bond. Characterization of a stable Ni^{I} species within a model protein has implications for understanding the mechanisms of complex enzymes, including acetyl coenzyme A synthase, and developing scaffolds for unique reactivity.

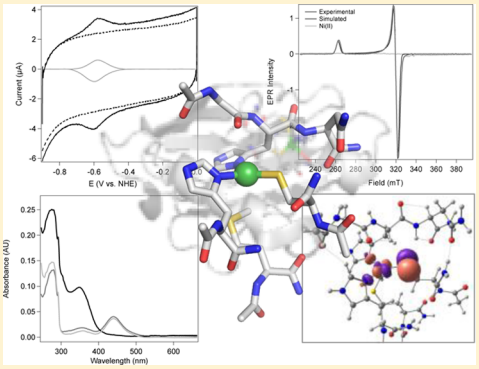

INTRODUCTION

Nickel metalloenzymes play important roles in managing global gas cycles, including regulation of atmospheric hydrogen, carbon monoxide, and methane by enzymes such as the [NiFe] hydrogenase (H2ase), monofunctional carbon monoxide dehydrogenase (CODH) and the CODH/acetyl coenzyme A synthase (ACS) complex, and methyl coenzyme M reductase (MCR), respectively.[1−4] Because these systems are highly relevant in the context of small molecule activation reactions and energy conversion processes, understanding their catalytic mechanisms is an important area of study. However, these enzymes typically require multiple cofactors and present experimental challenges due to oxygen sensitivity and elaborate biological assembly processes. Synthetic nickel compounds are also known to catalyze complex chemical bond formation and cleavage reactions; some of the most efficient compounds for hydrogen production and carbon dioxide fixation are based on mononuclear nickel centers, albeit with abiological ligands.[5−7] As an additional advantage, the resting states of nickel catalysts and proteins are often air-stable, suggesting that these systems could be applicable for large-scale reactions.

In both native metalloenzymes and small nickel complexes carrying out reductive chemistry, the +1 oxidation state is commonly invoked as a key catalytic intermediate. Ni^{I} compounds are electron-rich, typically low coordinate, and thus well-suited to bind inert molecules.[8] However, the potent reactivity of Ni^{I} species, while advantageous for effective chemistry, renders characterization challenging. One important tool in bioinorganic enzymology has been development of small molecules that serve as structural and/or functional models of the larger proteins. This avenue has been extensively explored using biomimetic ligands, and notable success has been achieved by a number of researchers for nickel proteins such as hydrogenase and superoxide dismutase.[9−14] Yet much remains poorly understood about the mechanisms of many other nickel enzymes, and the secondary and tertiary sphere interactions that the protein matrix provides cannot be ignored; these are often the subtle factors that dictate enzymatic selectivity and efficiency. ACS is one such enzyme, containing a dinuclear nickel site bridged by thiolate ligands and coupled to a [4Fe-4S] cluster (Figure 1).[15] Despite this complexity, only the nickel center proximal to the iron−sulfur cluster is involved in catalysis.[3,15−18] Small molecule compounds have been synthesized that are structurally and/or spectroscopically similar to the dinuclear nickel center of ACS but remain catalytically inactive.[19] These compounds vary in stability and often utilize abiological ligand platforms, with limited solubility

Received: May 15, 2015
Published: August 3, 2015

DOI: 10.1021/acs.inorgchem.5b01103
Inorg. Chem. 2015, 54, 7959−7967

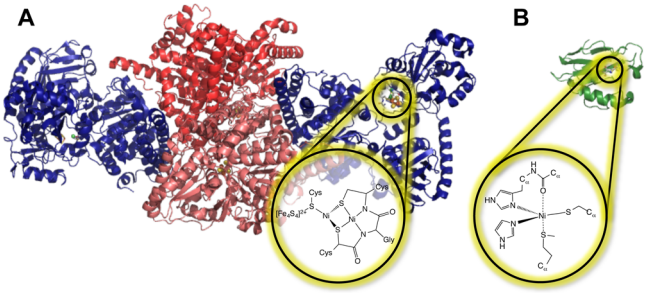

Figure 1. Ribbon structures and active-site diagrams of (A) carbon monoxide dehydrogenase/acetyl CoA synthase (PDB ID: 1OAO) and (B) azurin (PDB ID: 4AZU). Protein structures are shown to scale.

in aqueous solutions.[3,19,20] A structural mimic of nickel metalloenzyme active sites within a protein scaffold would provide distinct advantages over small molecule models. Native proteins fold into discrete structures with well-defined primary, secondary, and tertiary coordination environments, are easily manipulated via site-directed mutagenesis, and offer controlled substrate access.

For these reasons, azurin, a cupredoxin from *Pseudomonas aeruginosa*, has been selected as a scaffold for the design of model nickel proteins (Figure 1). Azurin is a robust protein that has received significant attention in the bioinorganic community due to its interesting spectroscopic features, electronic structure, tunable reduction potential, and rapid electron transfer kinetics.[21−24] Azurin is small, easily expressed, and highly tolerant to mutations, making it an attractive platform for use in protein engineering efforts.[25−27] Additionally, it is well-established that the active site can accommodate a variety of metals.[27−29] In many respects, azurin is an ideal candidate for developing structural and functional models of nickel metalloenzymes.

Here, we report that the incorporation of nickel into azurin creates a redox-active metalloprotein that serves as a model biological Ni^{I} system. Though nickel(II)-substituted azurin (Ni^{II}Az) has been known for many decades and studied using optical, vibrational, X-ray, and magnetic spectroscopies as well as X-ray crystallography,[28,30−33] the generation and characterization of other oxidation states within the protein has not been reported. Protein film electrochemistry shows reversible, fast electron transfer reflecting the $Ni^{II/I}$ couple, while optical and electron paramagnetic resonance spectroscopies demonstrate that reduced nickel(I)-azurin (Ni^{I}Az) is stable, isolable, and displays distinct features. Density functional theory calculations are used to probe the electronic structure. The covalent metal−thiolate bond, spectral signatures, and proposed trigonal planar geometry of the Ni^{I}Az active site resemble the electronic and geometric structures of the proximal nickel center in ACS.[15,34] These observations suggest that NiAz may serve as a model for intermediates in ACS and provide insight into understanding the ACS enzymatic mechanism.

MATERIALS AND METHODS

All materials were used as received unless otherwise noted.

Protein Expression and Purification. Expression and purification of azurin were carried out using standard heterologous protein expression techniques.[35] A summary of the protocol is given here. The pUC18 plasmid containing the gene for *Pae* wild-type (WT) azurin was received as a gift from Dr. Judy Kim, UCSD. The plasmid was transformed into BL21-DE3* competent *E. coli* expression cells (Life Technologies). An overnight starter culture of cells was grown in nutrient-rich Terrific Broth (TB) media containing 70 mg/L ampicillin (GoldBio Technologies) at 37 °C, 200 rpm, for 16 h, and then dispersed into 1 L flasks of TB media containing 70 mg/L ampicillin at 37 °C, 200 rpm, and grown for 4 h. Once the optical density reached ∼0.8, protein expression in the cells was induced using a 2 mM final concentration of IPTG (GoldBio Technologies). Following induction, the cells were maintained at 37 °C, 200 rpm, for 4−5 h. The cells were harvested by multiple rounds of centrifugation at 6800 × *g* for 5 min at 4 °C. The cell pellet was washed twice with 50 mM Tris-HCl buffer, pH 7.8, and stored at −80 °C until needed.

For lysis, cells were thawed and resuspended in 20 mM phosphate buffer, pH 7.2, containing 0.3 mg/mL of egg white lysozyme (BioBasic) and 20 μg/mL of bovine pancreas DNase I (Sigma-Aldrich). Lysis was allowed to proceed for 1.5 h at 22 °C. The resulting mixture was pelleted at 9800 × *g* for 30 min to remove cellular debris. The supernatant was decanted, and 1 M sodium acetate at pH 4.2 was added to bring the solution pH to 4.5. The acidified supernatant was centrifuged at 9800 × *g* for 30 min to pellet precipitated material. $Cu^{II}SO_4$ was added in excess to the supernatant to coordinate to apo-azurin, and a deep blue color developed within 5 min of copper addition. The supernatant was pelleted again at 9800 × *g* to remove any additional precipitate.

Cell extract was exchanged into 1 mM sodium acetate buffer at pH 4.5 and applied to a self-packed, 5 mL Source 15S cation exchange column (GE Amersham). The protein was eluted with a gradient of 300 mM sodium acetate buffer, pH 4.5, across a 100 mL elution gradient. Copper azurin eluted around 35%, which corresponded to ∼100 mM acetate. The purity of the resulting azurin was assessed using absorption spectroscopy; samples were determined to be pure if the A_{628}/A_{280} ratio was at least 0.5.[36] Blue fractions with ratios less than 0.5 were most likely a result of Zn contamination. SDS gel electrophoresis showed only a single band appearing at a molecular weight of ∼14 kDa (Supporting Information Figure S1) when compared to a protein ladder (Thermo Scientific Spectra Multicolor Low Range Protein Ladder).

Metal Substitution. Metal extraction and subsequent reconstitution was carried out as previously described.[35,37] Copper azurin (CuAz) was reduced using 3 mM sodium dithionite (Acros Organics) and dialyzed 3 times for 4 h each at room temperature against 400 mM potassium cyanide (Alfa Aesar) in 100 mM potassium phosphate buffer, pH 8.0 (Thermo Scientific Snakeskin dialysis tubing, MWCO 3.5 kDa), to extract all metals from the active site. ***Caution!*** *Potassium cyanide is a hazardous salt; therefore all solutions were handled in a fume hood at pH 8.0 or above to avoid the formation of toxic HCN gas.* The protein was then dialyzed against 100 mM potassium phosphate buffer, pH 8.0, twice, to remove any excess cyanide. After metal extraction, phosphate was removed by dialysis against 10 mM Tris buffer, pH 7.4, and metal reconstitution was achieved by dialysis against 7.5 mM $Ni^{II}SO_4$ or $Cu^{II}SO_4$ in 50 mM Tris, pH 7.4. Metalation with $Ni^{II}SO_4$ resulted in a yellow protein solution. Excess metal was removed by dialysis against 50 mM Tris, pH 7.4, and the protein was finally concentrated using centrifugal filtration devices (Millipore Centricons, MWCO 3.5 kDa). Optical properties of the nickel-substituted azurin were consistent with previously published reports.[28] Exhaustive cyanide dialysis as described here resulted in azurin containing less than 4% of the original copper, consistent with previously published results,[28] and near-quantitative generation of nickel-substituted azurin (NiAz), as verified by absorption spectroscopy using an extinction coefficient of 3300 M^{-1} cm^{-1} at 440 nm (Supporting Information Figure S2).[28] For example, after addition of a strong oxidant, such as hexachloroiridate, only 1 μM Cu^{II}Az contamination was observed in a 43 μM sample of Ni^{II}Az.

Preparation of Reducing Agents. The protocols used for preparation of titanium(III) citrate (Ti^{III}Cit) and europium(II) diethylene triamine pentaacetic acid (Eu^{II}DTPA) solutions were carried out with slight modifications to previously published procedures.[38] A $Eu^{II}Cl_2$ solution was prepared under a nitrogen atmosphere in an anaerobic glovebox (<10 ppm of O_2, Vigor Gas Technologies) by dissolution of solid $Eu^{II}Cl_2$ in 0.5 M HCl. The solution was brought to a final $Eu^{II}Cl_2$ concentration of 145 mM in 50

DOI: 10.1021/acs.inorgchem.5b01103
Inorg. Chem. 2015, 54, 7959−7967

mM Tris buffer, pH 8.0. A stock solution of DTPA was prepared at the same concentration by dissolution of solid DTPA into a 1:1 mixture of 1 M NaOH and 50 mM Tris pH 8.0. A 40 mM stock Eu^{II}DTPA solution was prepared using equal aliquots of the stock DTPA and $Eu^{II}Cl_2$ solutions. The potential of the Eu^{II}DTPA stock solution was measured using a 2-electrode system with a graphite working electrode and Ag/AgCl reference and found to be −1.10 V versus Ag/AgCl (−902 mV vs NHE).

Ti^{III}Cit was prepared using a modified procedure from the literature[39] in which 1 mL of $Ti^{III}Cl_3$ in 10% HCl solution (EMD Millipore) was added to 5 mL of 0.2 M sodium citrate. The solution was then neutralized with 4 mL of a saturated carbonate solution at pH 10.5 to bring the final mixture to a pH of 7.5. The potential of the 100 mM Ti^{III}Cit stock solution was measured using a 2-electrode system with a Pt working electrode and Ag/AgCl reference. Measured Ti^{III}Cit stock solution potentials were between −900 and −950 mV versus Ag/AgCl (−702 and −752 mV vs NHE).

UV−Vis. Absorption spectroscopy was carried out on a Shimadzu UV-2600 spectrophotometer. For the optical experiments, Ni^{II}Az was diluted to a final ∼15 μM concentration in 50 mM Tris-HCl, pH 8.0, under a nitrogen atmosphere in an anaerobic glovebox. Eu^{II}DTPA was added to a final concentration of 1 mM, which had a potential of −900 mV versus Ag/AgCl (−702 mV vs NHE). The cuvettes were stoppered to be gastight and measured against 50 mM Tris-HCl buffer, pH 8.0. A cuvette containing only buffer was used as a baseline to subtract from the Eu^{II}DTPA + protein sample, and for controls, samples of Eu^{II}DTPA and air-oxidized Eu^{III}DTPA in buffer were measured.

Electrochemistry. All electrochemical experiments were carried out using a WaveNow potentiostat (Pine Instruments) inside a glovebox under a nitrogen atmosphere. A standard three-electrode cell was used with a Ag/AgCl reference electrode (Pine Instruments), a platinum wire counter electrode, and a pyrolytic graphite edge-plane (PGE) working electrode, 3 mm diameter (CH Instruments). Potentials were measured against Ag/AgCl and converted to the normal hydrogen electrode (NHE) by the addition of +0.198 V to the measured potentials. Prior to experimentation, the PGE electrode was polished on a nylon polishing pad (Buhler) using a 1 μm alumina powder slurry and sonicated for 30 s in deionized water.[40] The electrode was then electrochemically activated by poising at −1 V for 30 s and cycling three times at 10 mV/s from −1 to 0 V. After reductive cleaning, 15 μL of 150 μM protein in 50 mM sodium acetate buffer, pH 4.5, was applied to the electrode surface using previously described methods.[40] Excess protein was pipetted off the electrode prior to immersion in the electrochemical cell. Cyclic voltammograms were initiated at the reductive limit. Quantitative analysis of electrochemical voltammograms was carried out using the SOAS program,[41] and the peak position dependence on scan rate was fit using the JellyFit software.[42] The electroactive coverage of protein on the electrode was determined by integration of the reductive and oxidative peaks in the CV and use of the following equation

$$I_{int} = N_A F \nu \Gamma \quad (1)$$

where N_A represents Avogadro's number, F represents Faraday's constant, ν represents scan rate, and Γ represents the electroactive coverage. Potentiometric titrations and pH-dependent electrochemical data were fit to the Nernst equation:

$$E = E^\circ - \frac{RT}{nF} \ln \frac{[\text{red.}]}{[\text{ox.}]} \quad (2)$$

EPR Spectroscopy. Continuous-wave (CW) X-band EPR spectra at 100 K were collected using a Bruker EMXPlus equipped with a Bruker variable temperature unit. CW X-band EPR spectra at 10 K were collected at the Ohio Advanced EPR Facility at Miami University using a Bruker EMX instrument equipped with an Oxford flow cryostat. Ni^{I}Az samples were prepared by adding an aliquot of Ti^{III}Cit to a solution of Ni^{II}Az in sodium acetate buffer, pH 4.5, to bring the mixture to a final concentration of 250 μM protein and 12 mM Ti^{III}Cit. The resultant solution potential was typically −750 mV versus Ag/AgCl (−552 mV vs NHE). Alternatively, Ni^{I}Az was prepared by adding an aliquot of Eu^{II}DTPA to a solution of Ni^{II}Az in sodium acetate buffer, pH 4.5, to bring the mixture to a final concentration of 200 μM protein and 3 mM Eu^{II}DTPA. The resultant solution potential was typically −875 mV versus Ag/AgCl (−677 mV vs NHE). After mixing, the samples were transferred into EPR tubes (Wilmad SQ-250M-4MM) and frozen in liquid nitrogen. EPR spectra were acquired for approximately 10 min with a microwave power of 2 mW at 100 K. A modulation frequency and amplitude of 100 kHz and 10 G, respectively, were used for all spectra. Spin quantitation was carried out using a Cu^{II}Az standard. The spectra were corrected for residual signals from the reducing agent using 1:1 subtractions, and a sloping baseline was removed using a linear spline fit in the Igor data analysis software. Control experiments with nickel salts and large excess concentrations of both reducing agents were used to demonstrate that the signals observed were due to the protein sample. EPR spectral simulations were carried out using the EasySpin software.[43]

DFT. All calculations were carried out with the computational chemistry software package ORCA.[44] Output files were analyzed using the ChemCraft program (www.chemcraftprog.com). A protein model of the active site was constructed using Pymol; initial coordinates were taken from the published crystal structure for nickel-substituted *Pseudomonas aeruginosa* azurin, PDB ID 1NZR.[30] The residues coordinated to the metal center were taken in their entirety along with with Asn47 and terminated with N-acetylation and C-amidation to build the cluster model used in all calculations. The Cartesian coordinates of the carbonyl carbon atoms on each residue were constrained, and only the S = 1 species for Ni^{II}Az was considered.[33] Geometry optimizations were carried out at the DFT level of theory using the BP86 functional with the RI approximation followed by the B3LYP functional with the RIJCOSX approximation.[45] Calculations employed the def2-TZVP basis set for nickel and directly coordinated atoms; remaining atoms were calculated using the def2-SV(P) basis set. Scalar relativistic effects were incorporated by the all-electron zeroth-order regular approximation (ZORA).[46] Dispersion effects were included using the atom-pairwise correction with Becke−Johnson damping as it has been adopted into the ORCA program (D3).[44] Dielectric effects of the enzyme environment were considered by embedding the model in a conductor-like screening model (COSMO) with a dielectric ε = 80 and shown to have little effect (Supporting Information Figure S22). The geometry-optimized Ni^{I}Az structure was also generated with the methods above; the same initial coordinates were used, and an additional electron was added to the system by modification of the charge and multiplicity.

The geometry-optimized structure of Ni^{I}Az was used to calculate EPR g-tensors, hyperfine couplings, spin density, and molecular orbitals. EPR parameters were calculated using the B3LYP functional; inclusion of the COSMO model and/or use of the PBE0 functional did not change the results (Supporting Information Table S1). Optical absorption spectra of both Ni^{I}Az and Ni^{II}Az were calculated via time-dependent DFT (TD-DFT) using the B3LYP functional and COSMO. Spin densities and molecular orbitals were generated and visualized using the orca_plot module.[44] A sample input file and optimized coordinates for Ni^{II}Az and Ni^{I}Az are given in the Supporting Information.

RESULTS

Protein Film Electrochemistry of NiAz. Protein film electrochemistry (PFE) provides a direct measurement of the thermodynamics and kinetics of electron transport in redox-active proteins and has been used extensively to characterize metalloenzyme activity.[47−49] It has been previously shown that CuAz readily forms monolayers on both pyrolytic graphite electrodes (PGE) and thiol-modified Au electrodes.[40,50,51] A protein film of NiAz was prepared by depositing a dilute solution of enzyme on the surface of the electrode, and excess solution was removed prior to insertion into the electrochemical cell.

DOI: 10.1021/acs.inorgchem.5b01103
Inorg. Chem. 2015, 54, 7959−7967

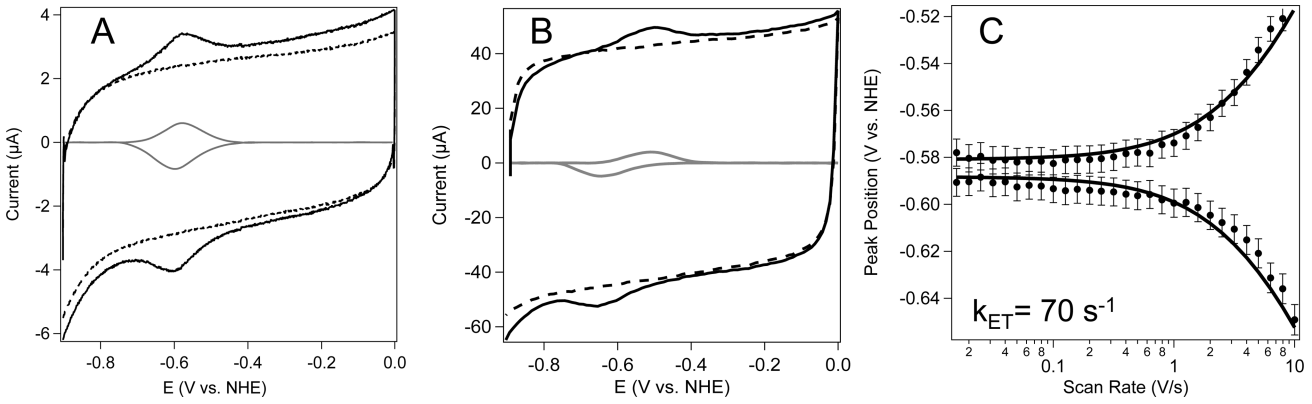

Figure 2. Cyclic voltammograms of immobilized NiAz (black) and CuAz (dashed) measured at (A) 500 mV/s and (B) 10 V/s. CVs were measured in a 50 mM sodium acetate buffer, pH 4.4, using a PGE working electrode. Inset voltammograms (gray) were baseline-subtracted and filtered using the SOAS analysis software.[31] (C) NiAz peak positions for anodic and cathodic waves measured from 15.8 mV/s to 10 V/s. Solid line represents best-fit to Butler–Volmer electron transfer kinetics generated using the JellyFit software;[42] error bars represent the range of values obtained from two independent measurements.

Cyclic voltammograms (CVs) of surface-adsorbed NiAz at pH 4.4 are shown in Figure 2. A reversible one-electron couple is observed at −590 mV versus NHE. Thus, substitution of copper, which has a reduction potential of 310 mV versus NHE under analogous conditions, with nickel lowers the reduction potential by 900 mV.[40,51] Despite this significant shift, only the native +II/+I redox couple is observed; no signals representing the $Ni^{III/II}$ transition could be seen. Integration of the peak area showed the electroactive coverage to be approximately 40 pmol/cm^2, consistent with prior reports;[40] control experiments using CuAz gave similar values (Supporting Information Figures S3–S5). The protein film was found to be stable under the conditions measured, with a desorption rate of 0.04 min^{-1} (Supporting Information Figure S3, inset).[40]

The CVs of NiAz were measured at varying scan rates, from 10 mV/s to 10 V/s. As the scan rate was increased, the oxidative and reductive peaks separate and broaden. A plot of peak position as a function of scan rate gives a characteristic "trumpet plot", which can be accurately modeled using Butler–Volmer electron transfer theory (Figure 2C).[42] From the best-fit parameters, an ET rate constant (k_{ET}) of 70 s^{-1} is obtained. The corresponding peak separations, best-fit simulations, and parameters for CuAz are shown in Supporting Information Figure S6, giving an ET rate constant of 1800 s^{-1}; this is consistent with prior studies on the electron transfer rates of CuAz on PGE, which report a value for k_{ET} of 1600 s^{-1}.[42]

For further comparison to CuAz, the reduction potential of NiAz was studied as a function of pH (Figure 3). As is often seen in redox proteins, the $Ni^{II/I}$ couple shifts to lower potentials as the pH is increased, with the midpoint potential shifting to −710 mV versus NHE at pH 8.0. However, attempts to fit the peak potential to typical Nernstian behavior resulted in poor fits (Supporting Information Figure S7). It is well-known that CuAz displays a pH-dependent reduction potential from pH 4 to pH 9, reflecting a complex proton-coupled electron transfer process due to interactions with His35.[51,52] This residue lies ∼8 Å from the metal center, and its effects on the reduction potential are attributed primarily to electrostatics. Because this residue is also present in NiAz, it is reasonable to assume those interactions would similarly influence the $Ni^{II/I}$ couple, though the impact of pH could be further complicated by the slower ET kinetics in NiAz.

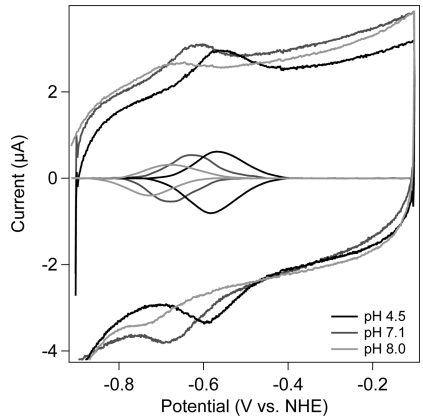

Figure 3. Cyclic voltammograms of immobilized NiAz at different pHs. CVs were measured using a PGE working electrode with a scan rate of 500 mV/s in 50 mM sodium acetate buffer, pH 4.5 (black), 50 mM PIPES buffer, pH 7.1 (dark gray), and 50 mM Tris buffer, pH 8.0 (light gray).

Absorption Spectroscopy. Removal of the native copper cofactor of Az and subsequent replacement with nickel results in the disappearance of the characteristic "blue" Cu^{II}Az charge transfer transition at 628 nm and the appearance of different bands (Supporting Information Figure S2). It has been suggested that the three charge transfer bands resulting from the incorporation of Ni^{II} into Az can be assigned to a $\pi_{SCys} \rightarrow Ni^{II}$ transfer at 560 nm, a $\sigma_{SCys} \rightarrow Ni^{II}$ at 440 nm, and a $\sigma_{SMet} \rightarrow Ni^{II}$ at 360 nm, implicating electronic interactions between the active-site Cys112 and Met121 residues and the metal center.[28] Titration of a strong one-electron reductant, such as Eu^{II}DTPA, into a dilute solution of Ni^{II}Az at pH 8.0 results in a decrease in absorbance of the characteristic Ni^{II}Az peaks and concomitant appearance of a new band at 350 nm (Figure 4). Upon exposure of the Ni^{II}Az + Eu^{II}DTPA sample to air, near-quantitative recovery of the absorption features at 440 and 360 nm was observed. Further support for the reversibility of this chemical reduction process is found in retention of the absorption shoulder at 292 nm due to the completely hydrophobic tryptophan-48.[35] That this band remains well-resolved under all conditions indicates that the protein remains properly folded.[53]

DOI: 10.1021/acs.inorgchem.5b01103
Inorg. Chem. 2015, 54, 7959–7967

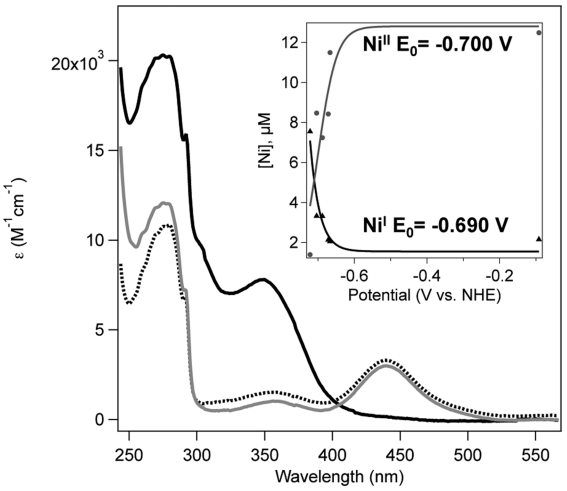

Figure 4. UV−vis absorption spectra of 15 μM Ni^{II}Az (gray), 15 μM Ni^{II}Az + 1 mM Eu^{II}DTPA (black), and 15 μM Ni^{II}Az + 1 mM Eu^{II}DTPA after reoxidation in air (dotted). Spectra were taken in 50 mM Tris buffer, pH 8.0, at room temperature. (Inset) Ni^{II}Az (gray) and Ni^{I}Az (black) concentrations as a function of potential. Solid lines represent fits to eq 2.

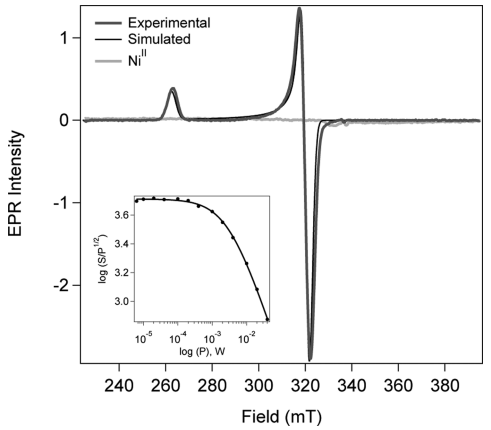

Figure 5. CW X-band experimental (gray) and simulated (black) EPR spectra of 200 μM Ni^{II}Az + 3 mM Eu^{II}DTPA in 50 mM Tris-HCl buffer, pH 8.0. Control Ni^{II}Az in buffer is shown in light gray. Measurements were conducted at 100 K, $P_{\mu w}$ = 2 mW, 10 G modulation amplitude. (Inset) Power saturation curve for Ni^{I}Az intensities measured at 10 K.

Weak spectral contributions from the absorption spectra of Eu^{II}DTPA and Eu^{III}DTPA were subtracted to isolate features due to the reduced Ni^{I}Az species (Supporting Information Figure S8). A full potentiometric titration with Eu^{II}DTPA (Supporting Information Figure S9) reveals that the decrease of the 440 nm band is correlated with the appearance of the band at 350 nm, and both are directly related to the potential of the solution. This relationship can be accurately modeled using the Nernst equation to yield a Ni$^{II/I}$ reduction potential of −695 mV at pH 8.0 (Figure 4, inset). The solution-phase reduction potential obtained from the absorption experiments is in close agreement with the potential observed by PFE at pH 8.0. These absorption features are absent in control experiments carried out with nickel salts + Eu^{II}DTPA or with reductant alone.

EPR Spectroscopy. Electron paramagnetic resonance spectroscopy was used to further characterize the reduced azurin species. Eu^{II}DTPA was added to a solution of Ni^{II}Az. The solution was frozen, and the CW EPR spectrum was measured at 100 K (Figure 5 and Supporting Information Figure S10). A highly anisotropic, axial signal with principal g-values of 2.56 and 2.10 was observed. Control experiments demonstrated that this signal did not originate from free nickel in solution (Supporting Information Figure S11). The EPR spectrum was easily simulated, and no additional features became apparent at lower temperatures or with an alternative reducing agent such as Ti^{III}Cit (Supporting Information Figures S13−S14). Spin quantification using a Cu^{II}Az standard revealed that approximately 75% of the initial sample concentration could be reduced. Full potentiometric titrations are shown in the Supporting Information (Figure S15) and are generally consistent with the reduction potentials obtained using electrochemical and spectrophotometric titrations. At very high concentrations of reducing agent, decreases in the EPR signal are observed that might be attributed to metal dissociation from azurin. Power saturation measurements at 10 K revealed a $P_{1/2}$ of 1.2 mW, with an inhomogeneous broadening parameter;[54] at 100 K, it was not possible to achieve saturation, though the signal was clearly visible. The resting state Ni^{II}Az has an S = 1 configuration and was not observed using conventional EPR techniques.

DFT. Density functional theory (DFT) calculations have been instrumental in facilitating interpretation of complex spectroscopic results and providing insight into the electronic structure of a wide variety of molecules, including metalloproteins.[33] DFT provides a compromise between computational expense and accuracy when modeling large systems.[55] Because it is well-established that the local environment and specific interactions around the active site play a critical role in determining the structure and function of metalloenzymes, DFT studies on NiAz were carried out using a cluster model that includes the metal, directly coordinated residues, and a modified secondary coordination sphere (Supporting Information Figure S16). Geometry optimization of the active site was carried out, and as has been done with other metalloenzymes, the cluster model was validated by verifying that the calculated geometric and spectroscopic markers of Ni^{II}Az were in agreement with experimental values.[56,57]

To generate the Ni^{I}Az structure, an electron was added to the system at the initial coordinates, and the geometry was reoptimized; the energy-minimized structure is shown in Figure 6. Interestingly, a considerable rearrangement of the active site appears to occur upon reduction. Ni^{II}Az has a distorted tetrahedral geometry with the M121 thioether coordinated to the metal with a Ni−S$_{Met}$ distance of 2.4 Å (Supporting Information Table S1). While this differs from the distance observed in the crystal structure (Supporting Information Figure S17), experimental measurements such as ^{1}H NMR pseudocontact shifts and the optical transitions suggest that M121 is bound to Ni^{II} in solution.[31] In Ni^{I}Az, the methionine residue is no longer coordinated to nickel; with a metal−ligand distance of 3.7 Å, the coordinated histidine residues rotate slightly, and the nickel center falls into the plane of the histidine and cysteine ligands to create a three-coordinate, trigonal planar active site (Figure 6 and Supporting Information Figure S18).

Time-dependent DFT calculations were run to predict the optical absorption spectrum of Ni^{I}Az (Figure 7). A hypsochromic shift of the dominant features upon reduction is predicted, with absorption cross sections that are similar to those of Ni^{II}Az. The calculated shift of ∼10 000 cm^{-1} is

DOI: 10.1021/acs.inorgchem.5b01103
Inorg. Chem. 2015, 54, 7959−7967

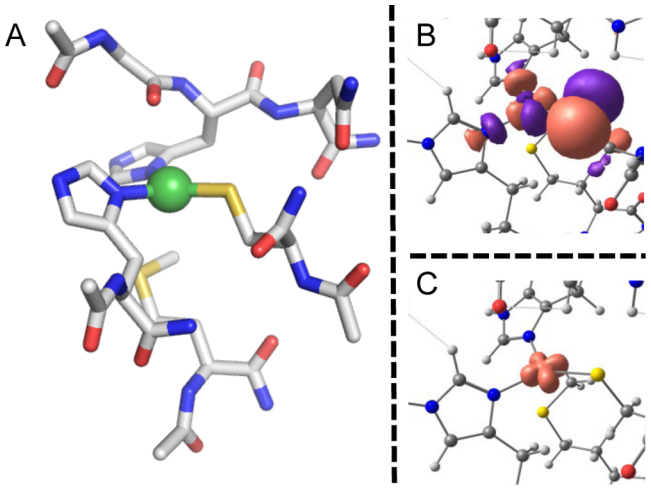

Figure 6. (A) Geometry-optimized structure of $Ni^{I}Az$. (B) Calculated SOMO of $Ni^{I}Az$. (C) Spin density distribution of $Ni^{I}Az$. All density plots were calculated using the geometry shown in part A.

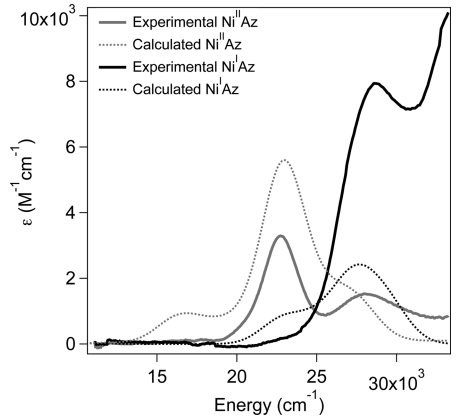

Figure 7. Experimental (—) and calculated (···) absorption spectra of $Ni^{I}Az$ (black) and $Ni^{II}Az$ (gray). Calculated transitions were convolved with a 3000 cm^{-1} Gaussian line width and offset by +5000 cm^{-1}.

comparable to that observed experimentally. Difference density plots of the most intense electronic transitions were generated and appear to be of metal-to-ligand charge transfer (MLCT) character, with the primary contribution to the π-system of His117 (Supporting Information Figure S19). These are distinct from the transitions predicted for $Ni^{II}Az$, which, as in $Cu^{II}Az$, are primarily LMCT bands from the π and σ systems of the cysteine and methionine sulfur atoms.

To further probe whether the DFT results were an accurate representation of the electronic structure of $Ni^{I}Az$, the g-tensor and hyperfine couplings to magnetic nuclei were calculated. The unique EPR properties observed experimentally, including axial symmetry, large anisotropy, and $g_{x,y} \neq g_e$, were all reproduced. The predicted g-values were 2.26, 2.11, and 2.10, independent of functional or the use of the COSMO model (Supporting Information Table S2), and the calculated isotropic superhyperfine couplings to the coordinated histidine nitrogens were 18 and 16 MHz. The calculated SOMO closely resembles the $d_{x^2-y^2}$ orbital with significant π^* involvement from the cysteine thiolate (Figure 6). The spin density is almost entirely localized on the metal center, with 89% found on nickel, 5% found on the cysteine thiolate, and the remaining 6% split between the two histidine ligands (Figure 6). A semiquantitative molecular orbital diagram is presented in the Supporting Information (Figure S20), showing that the canonical d-orbitals are essentially reproduced in the calculations.

DISCUSSION

Thermodynamics and Kinetics of $Ni^{I}Az$ Formation. The one-electron reduction of NiAz is observed at a potential approximately 1 V lower than that of the $Cu^{II/I}$ couple. While sizable, this shift is similar to differences in reduction potential between copper and nickel model compounds.[8] For example, the +II/+I couples of [14]aneN_4 macrocyclic compounds of copper and nickel are −660 and −1500 mV versus NHE, respectively.[58,59] Despite the extensive work done on metal substitution in azurin, this is the first time a new redox-active center has been reported in the wild-type coordination environment. Previous reports of iron substitution in azurin suggested that redox activity could only be achieved by altering the ligands in the binding site or using nuclear irradiation techniques such as cryoreduction.[27,60,61] Importantly, the $Ni^{II/I}$ couple remains physiologically accessible. Metalloenzymes containing low-valent nickel active sites have comparable reduction potentials, closely matched to the chemistry performed by those enzymes; the reduction potential of the proximal nickel center in ACS is observed at −540 mV.[3,62] The similarity in thermodynamics between the reduction of $Ni^{II}Az$ and the active-site Ni^{II} center in ACS highlights the potential utility of NiAz for related chemistry.

The kinetics of $Ni^{I}Az$ formation also differ significantly from those of $Cu^{I}Az$. The ET kinetics for reduction of NiAz by the PGE electrode are approximately 20-fold slower than those of CuAz. The protein orientations on the electrode are likely to be similar, given that the charge and electroactive coverage are independent of metal identity; thus, the decrease in k_{ET} likely derives from differences in internal reorganization energy for the ET process.[42,43] This would be consistent with a significant geometry change required for reduction, as predicted by DFT. However, CuAz is a highly optimized ET protein that exhibits one of the lowest reorganization energies (~0.7 eV) and some of the fastest self-exchange and intramolecular ET rates seen in nature, up to 10^6 M^{-1} s^{-1} and 10^6 s^{-1}, respectively.[25−6466] Thus, even with a 20-fold decrease in ET rate, relatively rapid electron transfer would still be accessible in NiAz, particularly from an optimized redox partner. Furthermore, catalytic processes involving redox reactions and heavy atoms are inherently slower than simple ET processes. Potential reactivity of the Ni^{I} site within azurin is likely to be limited by substrate transfer rates rather than electron transfer kinetics, as seen in other redox enzymes such as hydrogenase and ACS.[67] It is also reasonable to consider that solution-phase ET kinetics might differ from electron transfer to an electrode; this is clearly observed in CuAz PFE measurements.[40,68] Studies aimed at directly measuring the inherent reorganization energy of NiAz are currently underway.

Optical Absorption Features of $Ni^{I}Az$. The direct correlation between the reduction potential of NiAz observed using PFE and spectrophotometric titrations suggests that the intense optical band at 350 nm can be attributed to the absorption of $Ni^{I}Az$. This absorption feature is significantly blue-shifted from the dominant feature in $Ni^{II}Az$. An increase in energy upon reduction could be anticipated from a simple ligand-field argument and is further supported by TD-DFT calculations, as shown in Figure 7. Mapping the electronic

DOI: 10.1021/acs.inorgchem.5b01103
Inorg. Chem. 2015, 54, 7959−7967

transition difference densities for $Ni^{I}Az$ reveals that the dominant contribution to the MLCT band originates from a $Ni(d_{x^2-y^2}) \rightarrow His(p\pi)$ transition (Supporting Information Figure S19). The significant change in the nature of the electronic absorption spectrum, from an LMCT band in $Ni^{II}Az$ to an MLCT band in $Ni^{I}Az$, is attributed to the electronic and geometric rearrangement in the reduced state. Further confirmation of the nature of these transitions can be probed using resonance Raman excitation profiles and will be pursued in future experiments.

EPR Spectroscopy Reveals the Unusual Electronic Structure of $Ni^{I}Az$. The well-defined, highly anisotropic signal generated by reduction of $Ni^{II}Az$ shows axial symmetry and unusually high principal values of the *g*-tensor. These characteristics provide information on both the electronic and geometric structure of $Ni^{I}Az$. The $g_{x,y}$ values of 2.10 are significantly greater than 2, the value for a free electron (g_e); this indicates that the unpaired electron does not reside in the d_{z^2} orbital, which typically shows a *g*-value close to g_e.[69,70] With the observed $Ni^{I}Az$ *g*-tensor reflecting strong spin−orbit coupling, it can be assumed that the SOMO primarily consists of $d_{x^2-y^2}$ character, suggesting strong interactions with ligands in the *x*−*y* plane and no significant ligand−metal interactions along the *z*-axis. Thus, a significant degree of structural rearrangement likely occurs upon reduction. While both $Cu^{II}Az$ and $Ni^{II}Az$ have a slightly distorted, tetragonal active site (Supporting Information Figure S21), the EPR data suggests that the axial ligands are no longer coordinated in $Ni^{I}Az$, lowering the energy of the d_{z^2} orbital. Instead, the geometry of the active site likely resembles a trigonal planar species with the N_2S coordination from His46, His117, and Cys112 in a symmetric, pseudo-C_{3v} arrangement. Empirically, this would give rise to a $d_{x^2-y^2}$ SOMO, and this structure is further supported by DFT calculations, described below. As with $Cu^{II}Az$, at X-band frequencies, the superhyperfine coupling to the coordinated nitrogens is obscured (Supporting Information Figure S22 and Table S3); this broadening is thought to arise from *g*-strain introduced by the large anisotropy of the system.[71,72] The relaxation properties of $Ni^{I}Az$ also resemble those of $Cu^{II}Az$. Strong signal intensities are observed at high temperatures, indicating slow relaxation of the metal center; apparent signal saturation of the EPR spectrum was only observed at 10 K. The high signal intensities at modest temperatures suggest that detailed electronic structure characterization using pulsed EPR techniques may be tractable.[73]

While previously unobserved in azurin, a highly anisotropic signal with $g \neq g_e$ is seen in other low-coordinate biological Ni^{I} species. The Ni-L state in the [NiFe] hydrogenase, which features an open coordination site at the Ni^{I} center, shows an rhombic EPR signal with *g*-values of 2.30, 2.12, and 2.05; this transient, photogenerated state has recently been shown to be critically involved in catalysis.[74] In CODH/ACS, a transient intermediate generated by photolysis of the CO-coordinated Ni^{I}_{p} center has an essentially identical EPR spectrum to that of $Ni^{I}Az$, with *g*-values of 2.56 and 2.11.[34] This spectral resemblance highlights the structural similarity between $Ni^{I}Az$ and A*, despite their different coordination environments. There are also a handful of Ni^{I} inorganic and organometallic compounds with anisotropic EPR spectra;[8,59] an analogous electronic structure with a $d_{x^2-y^2}$ SOMO has been assigned to these species, though they are generally known to be relatively unstable.[75,76]

DFT Calculations Provide Structural Information on $Ni^{I}Az$. The close agreement between the experimental spectroscopic data and properties calculated using DFT supports the predicted geometric rearrangement in $Ni^{I}Az$. While $Ni^{I}Az$ has not previously been reported, the isoelectronic $Cu^{II}Az$ has been studied extensively using spectroscopic and theoretical techniques.[22] From these prior reports and the analysis presented here, the SOMO of $Ni^{I}Az$ resembles that of $Cu^{II}Az$ in terms of a strong π-bonding interaction between the 3p orbital of S_{Cys} and the $d_{x^2-y^2}$ orbital of $Ni^{I}Az$.[22] The delocalization and large orbital contribution from sulfur highlight the covalency of the metal−thiolate bond and indicate potential for ligand-centered reactivity, as has been seen in mutants of CuAz.[77]

Some differences are evident, however, between $Cu^{II}Az$ and $Ni^{I}Az$. $Cu^{II}Az$ remains in a pseudotetragonal coordination environment in both the Cu^{II} and Cu^{I} redox states, having weak interactions with the glycine carbonyl and methionine axial ligands, while $Ni^{I}Az$ appears to lose both of those axially coordinated ligands upon reduction, giving a trigonal planar species. Single-point calculations using the *in silico* reduced NiAz structure without geometry optimization predict an EPR spectrum that is rhombic, with *g*-values of 2.41, 2.32, and 2.13 that are inconsistent with experiment. The structural rearrangement required for reduction would also support a large reorganization energy for electron transfer relative to CuAz. This increased reorganization energy should decrease the electron transfer kinetics,[63] as discussed above. Taken together, the direct and indirect results from the DFT calculations are all in agreement with the experimental data, validating the structural assignments made.

$Ni^{I}Az$ as an Electronic Structure Mimic of CODH/ACS. CODH/ACS is a key enzyme for a number of anaerobes, responsible for the synthesis of the biological metabolite acetyl-CoA via the Wood−Ljungdahl pathway. The active sites of this multifunctional protein all contain nickel centers, both for the reversible binding and conversion of CO_2 to CO and for C−C bond formation between CO and a methyl group for acetyl transfer. Though some mechanistic details of these enzymes remain poorly understood, Ni^{I} species are thought to be involved in the catalytic cycles.[3]

Biomimetic compounds have played important roles in understanding the catalytic mechanisms of diverse metalloenzymes. However, in the case of CODH/ACS, generating models of the active sites in relevant redox states has proven challenging.[3,78] The work presented here suggests that NiAz can be considered a model for the proximal nickel center in the ACS subunit for the following reasons: (1) Two stable oxidation states, $Ni^{I}Az$ and $Ni^{II}Az$, are clearly identified; these are the minimal required redox states for the proposed "paramagnetic" enzymatic mechanism of ACS. (2) The EPR spectrum of $Ni^{I}Az$ is almost identical to that of a transient state in ACS, denoted A*. This state is competent for binding of both CO and a methyl group and has been implicated as a critical intermediate in catalysis. (3) The close resemblance between the spectral features of $Ni^{I}Az$ and A* indicates that the two species may share a similar geometric structure, thus providing support for the proposed trigonal planar coordination environment of A*.[3] The low-coordinate geometry and planarity of the active site in ACS allows coordination of two ligands, CO and a methyl group, on the same face. This binding motif enables the C−C bond coupling carried out by ACS, and, by analogy, has implications for the possible reactivity of NiAz.

DOI: 10.1021/acs.inorgchem.5b01103
Inorg. Chem. 2015, 54, 7959−7967

While the two systems have distinct primary coordination spheres, NiAz mimics the redox-active metal center in the ACS enzyme. As has occurred with the hydrogenase field, the development of an initial, biological model for ACS that reproduces spectroscopic features may lead to the establishment of models that are both structural and functional. Thus, further development of the NiAz platform can provide fundamental insight into the catalytic mechanism of this complex enzyme system.

CONCLUSIONS

In summary, we report that nickel-substituted azurin retains redox activity similar to that of the native cupredoxin. Electrochemical, optical, magnetic, and density functional theory investigations have been carried out for characterization of the stable Ni^{I} species. These analyses reveal that electron transfer rates remain relatively high despite significant geometric rearrangement of the active site in the reduced species. Comparison to nickel-containing enzymes and model compounds suggests that nickel-substituted azurin serves as an electronic structure mimic of the active-site nickel in acetyl-CoA synthase and may possess reactivity that has been previously inaccessible in biomimetic models. This work lays a foundation for development of NiAz as a structural and functional biological mimic of many complex metalloenzymes.

ASSOCIATED CONTENT

Supporting Information

Additional figures containing an SDS-PAGE gel, additional electrochemical data, UV−vis spectra, EPR spectra, DFT model coordinates, and a sample DFT input file. The Supporting Information is available free of charge on the ACS Publications website at DOI: 10.1021/acs.inorgchem.5b01103.

AUTHOR INFORMATION

Corresponding Author

*E-mail: shafaat.1@osu.edu.

Notes

The authors declare no competing financial interest.

ACKNOWLEDGMENTS

The authors would like to acknowledge the OSU Department of Chemistry and Biochemistry, the Ohio State University Institute for Materials Research, and the Ohio Supercomputer Center for support; Gary Lorigan and Rob McCarrick at the Ohio Advanced EPR Facility at Miami University for assisting with 10 K EPR experiments; James York-Winegar for assistance setting up calculations; and Prof. John Herbert, Jeffrey Slater, and Camille Schneider for helpful discussions.

REFERENCES

(1) Ragsdale, S. W. *J. Biol. Chem.* **2009**, *284*, 18571−18575.
(2) Lindahl, P. A. *J. Inorg. Biochem.* **2012**, *106*, 172−178.
(3) Can, M.; Armstrong, F. A.; Ragsdale, S. W. *Chem. Rev.* **2014**, *114*, 4149−4174.
(4) Lubitz, W.; Ogata, H.; Rüdiger, O.; Reijerse, E. *Chem. Rev.* **2014**, *114*, 4081−4148.
(5) Helm, M. L.; Stewart, M. P.; Bullock, R. M.; Rakowski-DuBois, M.; DuBois, D. L. *Science* **2011**, *333*, 863−866.
(6) Beley, M.; Collin, J.-P.; Ruppert, R.; Sauvage, J.-P. *J. Chem. Soc., Chem. Commun.* **1984**, 1315−1316.
(7) Froehlich, J. D.; Kubiak, C. P. *Inorg. Chem.* **2012**, *51*, 3932−3934.
(8) Lappin, A. G.; McAuley, A. In *Advances in Inorganic Chemistry*; Sykes, A. G., Ed.; Academic Press: New York, 1988; Vol. *32*, pp 241−295.
(9) Smith, S. E.; Yang, J. Y.; DuBois, D. L.; Bullock, R. M. *Angew. Chem., Int. Ed.* **2012**, *51*, 3152−3155.
(10) Barton, B. E.; Olsen, M. T.; Rauchfuss, T. B. *Curr. Opin. Biotechnol.* **2010**, *21*, 292−297.
(11) Dutta, A.; DuBois, D. L.; Roberts, J. A. S.; Shaw, W. J. *Proc. Natl. Acad. Sci. U. S. A.* **2014**, *111*, 16286−16291.
(12) Ito, M.; Matsumoto, T.; Tatsumi, K. *Inorg. Chem.* **2009**, *48*, 2215−2223.
(13) Shearer, J. *Acc. Chem. Res.* **2014**, *47*, 2332−2341.
(14) Broering, E. P.; Dillon, S.; Gale, E. M.; Steiner, R. A.; Telser, J.; Brunold, T. C.; Harrop, T. C. *Inorg. Chem.* **2015**, *54*, 3815−3828.
(15) Darnault, C.; Volbeda, A.; Kim, E. J.; Legrand, P.; Vernède, X.; Lindahl, P. A.; Fontecilla-Camps, J. C. *Nat. Struct. Biol.* **2003**, *10*, 271−279.
(16) Drennan, C. L.; Peters, J. W. *Curr. Opin. Struct. Biol.* **2003**, *13*, 220−226.
(17) Lindahl, P. A. *JBIC, J. Biol. Inorg. Chem.* **2004**, *9*, 516−524.
(18) Barondeau, D. P.; Lindahl, P. A. *J. Am. Chem. Soc.* **1997**, *119*, 3959−3970.
(19) Harrop, T. C.; Mascharak, P. K. *Coord. Chem. Rev.* **2005**, *249*, 3007−3024.
(20) Riordan, C. G. *JBIC, J. Biol. Inorg. Chem.* **2004**, *9*, 542−549.
(21) DeBeer, S.; Kiser, C. N.; Mines, G. A.; Richards, J. H.; Gray, H. B.; Solomon, E. I.; Hedman, B.; Hodgson, K. O. *Inorg. Chem.* **1999**, *38*, 433−438.
(22) Solomon, E. I.; Hadt, R. G. *Coord. Chem. Rev.* **2011**, *255*, 774−789.
(23) Marshall, N. M.; Garner, D. K.; Wilson, T. D.; Gao, Y.-G.; Robinson, H.; Nilges, M. J.; Lu, Y. *Nature* **2009**, *462*, 113−116.
(24) DiBilio, A. J.; Hill, M. G.; Bonander, N.; Karlsson, B. G.; Villahermosa, R. M.; Malmstrom, B. G.; Winkler, J. R.; Gray, H. B. *J. Am. Chem. Soc.* **1997**, *119*, 9921−9922.
(25) Hay, M.; Richards, J. H.; Lu, Y. *Proc. Natl. Acad. Sci. U. S. A.* **1996**, *93*, 461−464.
(26) Lancaster, K. M.; George, S. D.; Yokoyama, K.; Richards, J. H.; Gray, H. B. *Nat. Chem.* **2009**, *1*, 711−715.
(27) McLaughlin, M. P.; Retegan, M.; Bill, E.; Payne, T. M.; Shafaat, H. S.; Peña, S.; Sudhamsu, J.; Ensign, A. A.; Crane, B. R.; Neese, F.; Holland, P. L. *J. Am. Chem. Soc.* **2012**, *134*, 19746−19757.
(28) Tennent, D. L.; McMillin, D. R. *J. Am. Chem. Soc.* **1979**, *101*, 2307−2311.
(29) McLaughlin, M. P.; Darrah, T. H.; Holland, P. L. *Inorg. Chem.* **2011**, *50*, 11294−11296.
(30) Tsai, L.-C.; Sjölin, L.; Langer, V.; Bonander, N.; Karlsson, B. G.; Vänngård, T.; Hammann, C.; Nar, H. *Acta Crystallogr., Sect. D: Biol. Crystallogr.* **1995**, *51*, 711−717.
(31) Donaire, A.; Salgado, J.; Moratal, J.-M. *Biochemistry* **1998**, *37*, 8659−8673.
(32) Czernuszewicz, R. S.; Fraczkiewicz, G.; Zareba, A. A. *Inorg. Chem.* **2005**, *44*, 5745−5752.
(33) Funk, T.; Kennepohl, P.; Di Bilio, A. J.; Wehbi, W. A.; Young, A. T.; Friedrich, S.; Arenholz, E.; Gray, H. B.; Cramer, S. P. *J. Am. Chem. Soc.* **2004**, *126*, 5859−5866.
(34) Bender, G.; Stich, T. A.; Yan, L.; Britt, R. D.; Cramer, S. P.; Ragsdale, S. W. *Biochemistry* **2010**, *49*, 7516.
(35) Shafaat, H. S.; Leigh, B. S.; Tauber, M. J.; Kim, J. E. *J. Am. Chem. Soc.* **2010**, *132*, 9030−9039.
(36) Hutnik, C. M.; Szabo, A. G. *Biochemistry* **1989**, *28*, 3923−3934.
(37) Larson, B. C.; Pomponio, J. R.; Shafaat, H. S.; Kim, R. H.; Leigh, B. S.; Tauber, M. J.; Kim, J. E. *J. Phys. Chem. B* **2015**, *119*, 9438.
(38) Vincent, K. A.; Tilley, G. J.; Quammie, N. C.; Streeter, I.; Burgess, B. K.; Cheesman, M. R.; Armstrong, F. A. *Chem. Commun.* **2003**, 2590−2591.
(39) Zehnder, A. J.; Wuhrmann, K. *Science* **1976**, *194*, 1165−1166.
(40) Jeuken, L. J. C.; Armstrong, F. A. *J. Phys. Chem. B* **2001**, *105*, 5271−5282.

DOI: 10.1021/acs.inorgchem.5b01103
Inorg. Chem. 2015, 54, 7959−7967

(41) Fourmond, V.; Hoke, K.; Heering, H. A.; Baffert, C.; Leroux, F.; Bertrand, P.; Léger, C. *Bioelectrochemistry* **2009**, *76*, 141−147.
(42) Jeuken, L. J. C.; McEvoy, J. P.; Armstrong, F. A. *J. Phys. Chem. B* **2002**, *106*, 2304−2313.
(43) Stoll, S.; Schweiger, A. *J. Magn. Reson.* **2006**, *178*, 42−55.
(44) Neese, F. *Wiley Interdiscip. Rev. Comput. Mol. Sci.* **2012**, *2*, 73−78.
(45) Kossmann, S.; Neese, F. *J. Chem. Theory Comput.* **2010**, *6*, 2325−2338.
(46) van Lenthe, E.; Snijders, J. G.; Baerends, E. J. *J. Chem. Phys.* **1996**, *105*, 6505−6516.
(47) Armstrong, F. A.; Belsey, N. A.; Cracknell, J. A.; Goldet, G.; Parkin, A.; Reisner, E.; Vincent, K. A.; Wait, A. F. *Chem. Soc. Rev.* **2009**, *38*, 36−51.
(48) Léger, C.; Elliott, S. J.; Hoke, K. R.; Jeuken, L. J. C.; Jones, A. K.; Armstrong, F. A. *Biochemistry* **2003**, *42*, 8653−8662.
(49) Armstrong, F. A.; Hirst, J. *Proc. Natl. Acad. Sci. U. S. A.* **2011**, *108*, 14049−14054.
(50) Armstrong, F. A.; Heering, H. A.; Hirst, J. *Chem. Soc. Rev.* **1997**, *26*, 169−179.
(51) Yokoyama, K.; Leigh, B. S.; Sheng, Y.; Niki, K.; Nakamura, N.; Ohno, H.; Winkler, J. R.; Gray, H. B.; Richards, J. H. *Inorg. Chim. Acta* **2008**, *361*, 1095−1099.
(52) Jeuken, L. J. C.; Wisson, L.-J.; Armstrong, F. A. *Inorg. Chim. Acta* **2002**, *331*, 216−223.
(53) Petrich, J. W.; Longworth, J. W.; Fleming, G. R. *Biochemistry* **1987**, *26*, 2711−2722.
(54) Hirsh, D. J.; Brudvig, G. W. *Nat. Protoc.* **2007**, *2*, 1770−1781.
(55) *Metalloproteins*; Fontecilla-Camps, J. C., Nicolet, Y., Eds.; Humana Press: Totowa, NJ, 2014; Vol. *1122*.
(56) Kampa, M.; Pandelia, M. E.; Lubitz, W.; van Gastel, M.; Neese, F. *J. Am. Chem. Soc.* **2013**, *135*, 3915−3925.
(57) Krämer, T.; Kampa, M.; Lubitz, W.; van Gastel, M.; Neese, F. *ChemBioChem* **2013**, *14*, 1898−1905.
(58) Bernardo, M. M.; Heeg, M. J.; Schroeder, R. R.; Ochrymowycz, L. A.; Rorabacher, D. B. *Inorg. Chem.* **1992**, *31*, 191−198.
(59) Lovecchio, F. V.; Gore, E. S.; Busch, D. H. *J. Am. Chem. Soc.* **1974**, *96*, 3109−3118.
(60) Liu, J.; Meier, K. K.; Tian, S.; Zhang, J.; Guo, H.; Schulz, C. E.; Robinson, H.; Nilges, M. J.; Münck, E.; Lu, Y. *J. Am. Chem. Soc.* **2014**, *136*, 12337−12344.
(61) Davydov, R. M.; McLaughlin, M. P.; Bill, E.; Hoffman, B. M.; Holland, P. L. *Inorg. Chem.* **2013**, *52*, 7323−7325.
(62) Lindahl, P. A. *Biochemistry* **2002**, *41*, 2097−2105.
(63) Marcus, R. A.; Sutin, N. *Biochim. Biophys. Acta, Rev. Bioenerg.* **1985**, *811*, 265.
(64) Gray, H. B.; Winkler, J. R. *Annu. Rev. Biochem.* **1996**, *65*, 537−561.
(65) Gray, H. B.; Malmström, B. G.; Williams, R. J. P. *JBIC, J. Biol. Inorg. Chem.* **2000**, *5*, 551−559.
(66) Groeneveld, C. M.; Dahlin, S.; Reinhammar, B.; Canters, G. W. *J. Am. Chem. Soc.* **1987**, *109*, 3247−3250.
(67) Dementin, S.; Burlat, B.; Fourmond, V.; Leroux, F.; Liebgott, P. P.; Hamdan, A. A.; Leger, C.; Rousset, M.; Guigliarelli, B.; Bertrand, P. *J. Am. Chem. Soc.* **2011**, *133*, 10211−10221.
(68) Jeuken, L. J. C.; McEvoy, J. P.; Armstrong, F. A. *J. Phys. Chem. B* **2002**, *106*, 2304−2313.
(69) Potapov, A.; Lancaster, K. M.; Richards, J. H.; Gray, H. B.; Goldfarb, D. *Inorg. Chem.* **2012**, *51*, 4066−4075.
(70) Drago, R. S. *Physical Methods for Chemists*, 2nd ed.; Surfside Scientific Publishers: Gainesville, FL, 1992.
(71) Antholine, W. E.; Hanna, P. M.; McMillin, D. R. *Biophys. J.* **1993**, *64*, 267−272.
(72) Froncisz, W.; Hyde, J. S. *J. Chem. Phys.* **1980**, *73*, 3123−3131.
(73) Schweiger, A.; Jeschke, G. *Principles of Pulse Electron Paramagnetic Resonance*; Oxford University Press: Oxford, U.K., 2001.
(74) Hidalgo, R.; Ash, P. A.; Healy, A. J.; Vincent, K. A. *Angew. Chem., Int. Ed.* **2015**, *54*, 7110−7113.
(75) Horn, B.; Limberg, C.; Herwig, C.; Braun, B. *Inorg. Chem.* **2014**, *53*, 6867−6874.
(76) Wiese, S.; Kapoor, P.; Williams, K. D.; Warren, T. H. *J. Am. Chem. Soc.* **2009**, *131*, 18105−18111.
(77) Sieracki, N. A.; Tian, S.; Hadt, R. G.; Zhang, J.-L.; Woertink, J. S.; Nilges, M. J.; Sun, F.; Solomon, E. I.; Lu, Y. *Proc. Natl. Acad. Sci. U. S. A.* **2014**, *111*, 924−929.
(78) Ragsdale, S. W. *J. Inorg. Biochem.* **2007**, *101*, 1657−1666.

DOI: 10.1021/acs.inorgchem.5b01103
Inorg. Chem. 2015, 54, 7959−7967